



HAL
open science

Impact of biomineralization on the preservation of microorganisms during fossilization: An experimental perspective

Jinhua Li, Sylvain Bernard, Karim Benzerara, Olivier Beyssac, Thierry Allard, Julie Cosmidis, Julien Moussou

► To cite this version:

Jinhua Li, Sylvain Bernard, Karim Benzerara, Olivier Beyssac, Thierry Allard, et al.. Impact of biomineralization on the preservation of microorganisms during fossilization: An experimental perspective. *Earth and Planetary Science Letters*, 2014, 400, pp.113-122. 10.1016/j.epsl.2014.05.031 . hal-01050089

HAL Id: hal-01050089

<https://hal.science/hal-01050089>

Submitted on 9 Jan 2015

HAL is a multi-disciplinary open access archive for the deposit and dissemination of scientific research documents, whether they are published or not. The documents may come from teaching and research institutions in France or abroad, or from public or private research centers.

L'archive ouverte pluridisciplinaire **HAL**, est destinée au dépôt et à la diffusion de documents scientifiques de niveau recherche, publiés ou non, émanant des établissements d'enseignement et de recherche français ou étrangers, des laboratoires publics ou privés.

1 **Impact of biomineralization on the preservation of microorganisms during**
2 **fossilization: an experimental perspective**

3
4 Jinhua Li ^a, Sylvain Bernard ^{a,*}, Karim Benzerara ^a, Olivier Beyssac ^a, Thierry Allard ^a, Julie Cosmidis ^a,
5 Julien Moussou ^b

6
7 ^a *IMPMC, UMR 7590, CNRS, MNHN, UPMC, 4 place Jussieu, 75005 Paris, France*

8 ^b *École Normale Supérieure, Paris, France*

9
10 * Corresponding author.

11 E-mail addresses: lijinhua@mail.iggcas.ac.cn (J.H. Li), sbernard@mnhn.fr (S. Bernard),
12 karim.benzerara@impmc.upmc.fr (K. Benzerara), olivier.beyssac@impmc.upmc.fr (O. Beyssac)

13

14 **ABSTRACT**

15 The biogenicity of fossil microbial biomorphs is often debated because their morphologies are poorly
16 informative and the chemical, structural and isotopic signatures of biogenic organic molecules have been
17 altered during their incorporation into the sediments and the geological history of the host rock. Here, we
18 investigated the effect of encrustation by biominerals on the morphological and chemical degradation of
19 *Escherichia coli* cells during experimental thermal treatments with the aim of simulating fossilization
20 processes. Non-calcified *E. coli* cells and *E. coli* cells encrusted by calcium phosphates were exposed to
21 heating under an Argon atmosphere at two different temperatures (300°C, 600°C) for different durations
22 (2 h, 20 h, 100 h). Products were characterized down to the nm-scale using a combination of scanning
23 electron microscopy, transmission electron microscopy, Raman microspectroscopy, electron
24 paramagnetic resonance (EPR) spectroscopy, Fourier transform infrared (FT-IR) spectroscopy and
25 scanning transmission X-ray microscopy. In absence of encrusting biominerals, the morphological
26 structure of *E. coli* cells was completely lost after heating at 300 or 600°C, even after short (2h) heating
27 experiments. *E. coli* cells heat-treated at 600°C for 20 h had an increased content of aromatic functional
28 groups, and the amide functional groups were lost. Moreover, the EPR spectrum of these cells showed a
29 supra-Lorentzian line shape, similar to the EPR spectrum of organic carbon detected in the Apex chert (ca.
30 3460 Myr) for example. In contrast, calcified *E. coli* exposed to the same conditions (300 or 600°C)
31 showed limited morphological alteration as observed by electron microscopies and less chemical
32 transformation as detected by FT-IR and EPR spectroscopies. These experiments evidence the strong
33 influence of cell encrustation by minerals on their preservation potential during fossilization processes.

34

35 **Keywords:** Experimental taphonomy, Biomineralization, Fossilization, Exceptional preservation, EPR,
36 FT-IR

37 **1. Introduction**

38 A wide diversity of microorganisms can form a variety of crystalline or amorphous biominerals via
39 biomineralization within their cells, in their cell walls, at the cell surface, on extracellular structures and
40 away from the cells (e.g., Lowenstam, 1981; Weiner and Dove, 2003; Konhauser and Riding, 2012).
41 These biomineralization processes are relatively fast and can occur in a few hours or days (e.g., Miot et al.,
42 2009; Chan et al., 2011), resulting in the formation of diverse organo-mineral complexes including
43 biominerals and biomineral-encrusted cells/biostructures (Li J. H. et al., 2013). Recent analytical
44 advances offer promises to characterize chemically and mineralogically these complexes down to the nm-
45 scale (e.g., Miot et al., in press). Encrustation of microbial cells by biominerals can be seen as a first stage
46 of fossilization (e.g., Oehler and Schopf, 1971; Westall, 1995; Toporski et al., 2002; Benning et al., 2004;
47 Lalonde et al., 2005; Miot et al., 2009; Orange et al., 2009; Li et al., 2010; Chan et al., 2011). It has often
48 been hypothesized that biomineral-encrusted cells/biostructures may be more resistant to diagenesis
49 and/or metamorphism than pure organic molecules and structures, and therefore that they may be better
50 preserved over geological timescales (see Li J. H. et al., 2013 for a review). Yet, such assumptions have
51 not yet been evidenced experimentally.

52 Assessing the biogenicity of microbial-like structures in ancient rocks is challenging since the
53 original biological information they contain can be significantly altered during fossilization processes
54 (e.g., Gourier et al., 2004; Vandenbroucke and Largeau, 2007; Papineau et al., 2010), and these
55 biostructures may thus be mistaken with abiotic structures (Brasier et al., 2002; García-Ruiz et al., 2003;
56 Van Zuilen et al., 2007; Cosmidis et al., 2013). In addition, determining unambiguously the syngenecity
57 of putative microfossils within a rock requires a precise assessment of the thermal history that they have
58 experienced (Brasier and Wacey, 2012).

59 Exposing modern microorganisms in the laboratory to well-constrained temperature conditions may
60 help improving our knowledge on the transformations of such fossils induced by burial and maturation
61 processes (Li J. H. et al., 2013). Such experiments have been used increasingly to study the thermal
62 maturation of biomolecules or biominerals under various pressure and temperature conditions (e.g.,
63 Stankiewicz et al., 2000; Gupta et al., 2006; Skrzypczak-Bonduelle et al. 2008; Watson et al., 2012;
64 Bourbin et al., 2013; Li Y. L. et al., 2013). For instance, Skrzypczak-Bonduelle et al. (2008) reported the
65 continuous evolution of electron paramagnetic resonance (EPR) line shapes gradually from a Gaussian-
66 Lorentzian to a supra-Lorentzian profile for organic matter experiencing step-heating from room
67 temperature up to 800°C, similarly to what is reported for field samples. Similar results were recently
68 obtained by Bourbin et al. (2013) on bacteria heat-treated in the laboratory, thereby confirming that EPR
69 spectroscopy provides a powerful tool to study the geochemical maturity of organic matter.

70 However, comparing extant microbes or biominerals with putative ancient microfossils or fossil
71 biominerals is still a challenge as the impact of mineral encrustation on the preservation of microbial
72 fossils has not yet been tested in detail (Li J. H. et al., 2013). Here, we report results of thermal
73 degradation experiments performed on *Escherichia coli* cells with or without Ca-phosphate encrusting
74 their cell walls at 300 and 600°C under argon atmosphere for various durations (up to 100 h). Thermally
75 degraded cells were characterized using scanning electron microscopy (SEM), transmission electron
76 microscopy (TEM), Raman microspectroscopy, EPR spectroscopy, Fourier-Transform infrared
77 spectroscopy (FT-IR) and scanning transmission X-ray microscopy (STXM) coupled with X-ray
78 absorption near edge structure (XANES) spectroscopy. These techniques are highly complementary.
79 While Raman spectroscopy is sensitive to the organization of the aromatic skeleton in carbonaceous
80 material (e.g., Beyssac et al., 2003; Lahfid et al., 2010; Beyssac and Lazari, 2012), EPR spectroscopy
81 detects the electron spin of organic radicals in carbonaceous matter with high sensitivity (e.g., Mrozowski,
82 1988; Bourbin et al., 2013), C-XANES spectroscopy provides information on organic carbon speciation
83 (e.g., Bluhm et al., 2006; Solomon et al., 2009), and FT-IR spectroscopy allows identifying the different
84 chemical bonds within organic molecules (e.g., Yule et al., 2000).

85

86 **2. Materials and methods**

87 **2.1 Sample preparation**

88 Calcium-phosphate encrusted (i.e., calcified) and non-encrusted (i.e., non-calcified) *E. coli* cell
89 samples used in the present study were derived from the same *E. coli* Apm1 strain. Strain Apm1 was
90 obtained by transformation of *E. coli* BL 21 cells by the pET gene expression system (Studier and Moffatt,
91 1986). This plasmid contained (i) a *phoA* gene coding for an alkaline phosphatase linked to a promoter
92 activated by isopropyl β -D-thiogalactoside (IPTG), and (ii) an ampicillin resistance marker. The addition
93 of IPTG to the culture medium induced the transcription of the *phoA* gene, resulting in the over-
94 expression of alkaline phosphatase enzymes (PHO A). Encrustation of the cells by Ca-phosphates was
95 achieved by culturing cells over-expressing PHO A in a calcification medium.

96 To obtain cells encrusted by Ca-phosphates, cells from one single colony grown on LB agar medium
97 (Sigma-Aldrich Co.), were inoculated within 5 ml of autoclaved liquid LB medium (Sigma-Aldrich Co.)
98 and grown overnight at 37°C and 180 rpm. This 5-ml culture was transferred into 500 ml of liquid LB for
99 bacterial amplification culture. This culture was also carried out at 37°C and 180 rpm; the optical density
100 at 600 nm (OD₆₀₀) was monitored during the growth. Once the OD₆₀₀ reached a value between 0.6 and 0.8
101 after ~4-6 h incubation (corresponding to the exponential growth phase of *E. coli* cells), 1 ml of IPTG
102 (0.4 mM) was added to induce the overexpression of the *phoA* gene, leading to the production by the cells
103 of high amounts of PHO A. After 4-hours of incubation under these conditions, cells were harvested by

104 centrifugation at 6500 rpm for 15 min and rinsed three times with distilled water. Cells were then
105 transferred to 2 liters of a calcification medium and incubated at 37°C with shaking at 120 rpm. The
106 calcification medium, specifically designed to favor encrustation by Ca-phosphates, was prepared by
107 dissolving calcium-glycerophosphate (glycerol phosphate calcium salt, Sigma-Aldrich Co.) in a HEPES
108 (4-(2-hydroxyethyl)-1-piperazineethanesulfonic acid) pH-buffer (20 mM). HCl (1M) was used to adjust
109 the pH to 7.5 and the medium was sterilized by filtration through a 0.22- μ m filter. After a week, the
110 incubated cells, completely encrusted by Ca-phosphates were centrifuged at 8000 rpm for 15 min and
111 rinsed three times in distilled water.

112 To obtain the non-encrusted *E. coli* cells, 2-ml suspension of precultured Apm1 were transferred into
113 1 liter of liquid LB medium and allowed to grow overnight, and then harvested by centrifugation and
114 rinsed with distilled water using the same protocol as for the calcified *E. coli*.

115 All media contained a final concentration of ampicillin of 50 μ g·ml⁻¹ to prevent growth of potential
116 contaminants.

117

118 **2.2 Thermal treatments**

119 Calcified and non-calcified *E. coli* cells were first dehydrated at ambient temperature in a vacuum
120 dryer for two weeks at ambient temperature (i.e. ~20°C), and then heat-treated at different temperatures
121 (i.e., 300 and 600°C) for various durations (i.e., 2, 20 and 100 h) in an inert Argon atmosphere using a
122 Carbolite single zone horizontal tube furnace (GHA12/300) equipped with a Quartz work-tube. For all
123 experiments, the increase of temperature followed a constant ramp of 5°C·min⁻¹. Experimental solid
124 products were characterized using SEM and TEM while their chemical, structural and molecular
125 signatures were analysed by Raman, EPR, XANES and FT-IR spectroscopies.

126

127 **2.3 SEM and TEM**

128 Experimental solid products were finely ground in distilled water. Samples for SEM were deposited
129 on cover slides (~3 mm × 3 mm) mounted on aluminum SEM stubs with high-conductivity copper tape.
130 Samples for SEM were coated with carbon or gold. SEM observations were performed on a Zeiss Supra
131 55 SEM microscope at a 10 kV accelerating voltage and a working distance of 7.5 mm. SEM images were
132 collected with both in-Lens and Angle selective Backscattered (AsB) detectors. Samples for TEM
133 analyses were deposited on carbon coated Formvar grids. TEM experiments were carried out on a JEOL-
134 2100F microscope operating at 200 kV, equipped with a field emission gun, an ultra high-resolution
135 (UHR) pole piece, a Gatan energy filter GIF 200, a JEOL detector with an ultrathin window allowing
136 detection of light elements, and a scanning TEM (STEM) device, which allows Z-contrast imaging in

137 high angle annular dark field (HAADF) mode. Elemental mapping was acquired by EDXS (energy
138 dispersive X-ray spectroscopy) in the STEM mode.

139

140 **2.4 Raman spectroscopy**

141 Raman data were obtained on powders with a Renishaw INVIA microspectrometer as described in
142 Bernard et al. (2008). Spectra were measured from 500 to 3500 cm^{-1} at constant room temperature using
143 the 514.5 nm wavelength of a 50 mW Modulaser Argon laser (green laser) focused on the sample through
144 a Leica DMLM microscope with a long working distance 50X objective (NA = 0.55). This configuration
145 yielded a planar resolution of $\sim 1 \mu\text{m}$ for a laser power delivered at the sample surface set at around 250
146 μW to prevent irreversible thermal damage that could be due to laser-induced heating (Beyssac et al.,
147 2003). Light was dispersed by a grating with 1800 lines/mm and the signal was analyzed with a
148 RENCAM CCD detector. Measurements were performed with a circularly polarized laser using a $\frac{1}{4}$
149 wavelength plate placed before the microscope in order to limit polarization effects. The collected Raman
150 signal was fitted using the procedure introduced by Lahfid et al. (2010). Additional Raman analyses were
151 performed using the 785 nm wavelength of a 300mW Renishaw diode laser (near-infrared laser) with a
152 planar resolution of $\sim 2\text{-}3 \mu\text{m}$ and low laser power. As this configuration did not improve the signal-to-
153 fluorescence ratio, only data collected using the green laser are presented here.

154

155 **2.5 EPR spectroscopy**

156 EPR data were collected on powders at room temperature at the X-band (9.86 GHz) using a
157 BRUKER EMX spectrometer with the following parameters: center field 3530 G, modulation frequency
158 100 kHz, microwave power 1 mW, and modulation amplitude 0.3 G. The spectrometer was calibrated
159 using the diphenylpicrylhydrazyl (DPPH) standard with a known g factor ($g = 2.0037$). As the detection
160 scheme of EPR gave spectra in the forms of a first derivative of the EPR absorption, a plot of
161 $[A_{pp}\Delta B/(\Delta B_{pp}A)]^{1/2}$ versus $(\Delta B/\Delta B_{pp})^2$ was used to further characterize the line shape by its deviation from
162 a pure Lorentzian line, where ΔB_{pp} and A_{pp} are the peak-to-peak line width and amplitude, respectively,
163 ΔB is the magnetic field offset from this line center, and A is EPR amplitude values at each point of the
164 EPR line (Skrzypczak-Bonduelle, 2008). The line shape parameter R_{10} , which quantified the deviations of
165 the experimental points from the Lorentzian shape in this plot, was calculated following Skrzypczak-
166 Bonduelle et al. (2008).

167

168 **2.6 STXM-based XANES spectroscopy**

169 Experimental solid products were finely ground and deposited on Si_3N_4 windows for STXM
170 analyses. XANES data were collected on beamline 5.3.2.2 (STXM Polymer beamline - Kilcoyne et al.,

171 2003) at the Advanced Light Source (ALS) and beamline 10ID-1 (SM beamline - Kaznatcheev et al.,
172 2007) at the Canadian Light Source (CLS). Beamline 5.3.2.2 (ALS) works in the soft X-ray energy range
173 (250 - 800 eV) and is based on a bending magnet. The ALS storage ring was operated at 1.9 GeV and 500
174 mA current in a top-up mode. Beamline 10ID-1 (CLS) works in the soft X-ray energy range (130 - 2500
175 eV) and is based on an elliptically polarized undulator (EPU). The CLS storage ring was operated at 2.9
176 GeV and between 100 and 250 mA current. On both beamlines, the microscope chamber was first
177 pumped down to 100 mTorr after sample insertion and back-filled with He.

178 Rationale for the use of STXM to study biominerals can be found in Cosmidis and Benzerara (2014).
179 Energy calibration was accomplished using the well-resolved 3p Rydberg peak at 294.96 eV of gaseous
180 CO₂ for the C K-edge. Alignment of images of stacks and extraction of XANES spectra were done using
181 the aXis2000 software (ver2.1n). Normalization and assessment of spectral peak positions were
182 determined using the Athena software package (Ravel and Newville, 2005). Extensive databases of
183 reference C-XANES spectra were available from the literature (e.g., Solomon et al., 2009).

184

185 **2.7 FT-IR Spectroscopy**

186 Experimental solid products were finely ground, diluted within dried potassium bromide (KBr), and
187 pressed under 8 tons of pressure for 1 min to be characterized by FT-IR spectroscopy. FT-IR spectra were
188 recorded between 400 and 4000 cm⁻¹ with a resolution of 0.5 cm⁻¹ by using a Nicolet 7600 FT-IR
189 spectrometer. Two hundred absorbance spectra were obtained and averaged for each sample.

190

191 **3. Results**

192 **3.1 Electron microscopy**

193 After dehydration, non-calcified Apm1 cells display a rod-shaped morphology typical of *E. coli* cells,
194 with a width of ~0.5-0.8 μm and a length of ~1-3 μm (Fig. 1a). In contrast, calcified Apm1 cells appear as
195 large aggregates of cells encrusted heavily by calcium phosphates that can be observed at the cell surface
196 as well as within the cells and the cell walls (Fig. 1c and Fig. S1a-c). STEM-EDXS mapping, HRTEM
197 imaging, and selected area electron diffraction (SAED) analyses reveal that these calcium phosphates are
198 poorly crystalline with d-spacing values (e.g., 3.46 Å and 2.73 Å) consistent with those of hydroxyapatite
199 (HA) (Cuisinier et al., 1987) (Fig. S1d-k).

200 Cell structures of non-calcified *E. coli* were completely disrupted after all heat-treatments, including
201 at 300°C for 2 h (Fig. 1b). In contrast, calcified *E. coli* cells appeared well preserved morphologically
202 after all thermal degradation experiments, including heat-treatment at 600°C for 20 h (Fig. 1d). The
203 morphological and chemical features of calcified *E. coli* cells and their associated minerals remained
204 relatively constant upon heating as evidenced by SEM, TEM and STEM-EDXS analyses except for the

205 crystallinity of calcium phosphates, which increased with temperature as shown qualitatively by SAED
206 and HRTEM analyses (Fig. S2).

207

208 **3.2 Raman and EPR spectroscopy**

209 Raman microspectroscopy is sensitive to the organization of the aromatic skeleton in graphitic
210 carbons at the micrometer-scale (Bernard et al., 2010), while EPR spectroscopy is a bulk technique
211 sensitive to the physiochemical structures of aromatic radical moieties (Mrozowski, 1988). These two
212 techniques were used to characterize the solid products obtained after various thermal degradation
213 experiments. However, the very high fluorescence overwhelming the Raman signal prevented collecting
214 Raman data on most of the experimental solid products except for non-calcified *E. coli* cells heated at
215 600°C for 20 h (Fig. 2a). The Raman spectrum of this sample exhibited two dominant broad features
216 centered at about 1360 and 1605 cm^{-1} . These two features could be assigned to the main defect D1 band
217 centered at 1355 cm^{-1} , and to a composite band including the graphite G and the D2 defect bands.
218 Additionally, an intense D3 defect band centered at $\sim 1515 \text{ cm}^{-1}$ was clearly present. Such a spectrum was
219 highly similar to the Raman spectra of partially combusted organic compounds such as soots, charcoals or
220 organic residues of wood fires (e.g., Paris et al., 2005; Sadezky et al., 2005).

221 X-band EPR spectra were collected on both calcified and non-calcified *E. coli* cells heat-treated at
222 600°C for 20 h (Fig. 2b). Although both samples were characterized by the same EPR center ($\sim 3535 \text{ G}$),
223 they exhibited different EPR spectra in terms of line shape and width. The line width parameter ΔB_{pp} was
224 0.246 mT for non-calcified *E. coli* cells heated at 600°C for 20 h and 0.441 mT for calcified *E. coli* cells
225 heated at 600°C for 20 h. The EPR line shape of heated calcified *E. coli* cells was a combination of
226 Gaussian and Lorentzian profiles with a R_{10} factor of 0.82, while the heated non-calcified *E. coli* cells
227 exhibited a supra-Lorentzian EPR line shape (close to 2-D dipolar) with a R_{10} factor of -1.85 (Fig. 2c),
228 typical of more mature natural organic matter (Skrzypczak-Bonduelle et al., 2008; Bourbin et al., 2013).

229

230 **3.3 STXM-based XANES spectroscopy**

231 STXM-based XANES spectroscopy was used to document the evolution of carbon speciation in non-
232 calcified *E. coli* cells heated at increasing temperatures for various durations (Fig. 3). STXM
233 measurements could not be performed on calcified *E. coli* cells since they were opaque to X-rays because
234 of heavy encrustation.

235 The C-XANES spectrum of non-heated and non-calcified *E. coli* cells was similar to the spectra
236 measured for other bacteria by previous studies (e.g., Benzerara et al., 2004; Miot et al., 2009; Li J. H. et
237 al., 2013), with a main peak at 288.2 eV, attributed to $1s \rightarrow \pi^*$ electronic transitions of carbon in amide
238 groups, a peak at 285.2 eV, attributed to electronic transitions of carbon in aromatic or olefinic carbon

239 groups (C=C) and two additional peaks at 287.3 eV and 289.4 eV, attributed to $1s \rightarrow \pi^*$ electronic
240 transitions of carbon in hydroxyl (C-OH) functional groups associated with phenols, and aryl ethers or
241 hydroxylated aromatics and $C1s \rightarrow 3p/\sigma^*$ electronic transitions of carbon in hydroxylated- or ether-linked
242 carbon species, respectively (Solomon et al., 2009).

243 The intensity and the width of the peak at 285.2 eV progressively increased with increasing heating
244 duration at 300°C, while the intensity of the peak at 288.2 eV decreased and its width increased. The
245 broadening of the peak at 288.2 eV might be related to the increase of aliphatic and carboxylic group
246 contents, which have major absorption peaks at 287.8 eV and 288.5 eV, respectively.

247 With increasing temperature, the spectral evolution of heat-treated non-calcified *E. coli* cells was
248 even more pronounced. At 600°C, the peak at 288.2 eV almost disappeared, suggesting massive loss of
249 amide functional groups. Based on C-XANES spectra, non-calcified *E. coli* cells heat-treated at 600°C
250 were composed of aliphatic-rich organic molecules dominated by poorly condensed aromatic structures
251 (Solomon et al., 2009).

252

253 **3.4 FT-IR spectroscopy**

254 Non-calcified and non-heated *E. coli* cells showed a FT-IR spectrum very similar to spectra of
255 bacteria reported in the literature (e.g., Filip et al., 2008). Three major peaks could be observed at 1655
256 cm^{-1} , 1540 cm^{-1} , and 1237 cm^{-1} and were attributed based on previous studies to amide I, amide II, and
257 amide III vibrational modes, respectively (Fig. 4a). Noticeably, C-O and C=C stretchings may also
258 contribute to these peaks. The band at 1455 cm^{-1} was assigned to C-H deformations of CH_2 or CH_3 groups
259 in aliphatics; the band at 1393 cm^{-1} to C-H bending ($-\text{CH}_3$ stretch in fatty acids); the band at 1082 cm^{-1} to
260 C=O asymmetric stretching (glycopeptides, ribose, aliphatic esters), and the band at 2958-2854 cm^{-1} to C-
261 H stretching in aliphatics of cell walls (fatty acids, carbohydrates) (e.g., Filip et al., 2004 and references
262 therein). Consistently with C-XANES data, the FT-IR spectra of heat-treated non-calcified *E. coli* cells
263 varied with increasing temperature indicating some chemical transformation of the organic carbon
264 composing the cells: the peaks of amide (1655 cm^{-1} , 1540 cm^{-1} , and 1237 cm^{-1}), aliphatics (2958-2854
265 cm^{-1} , 1455 cm^{-1} , and 1393 cm^{-1}) and carbonyl or carboxyl groups (1082 cm^{-1}) progressively disappeared
266 when samples were heated up to 600°C. Peaks at 1628 cm^{-1} , 1702 cm^{-1} and 1265 cm^{-1} , assigned to
267 aromatic C=C, C-O bonds of CO_2H groups and C=O bonds of COOH groups, respectively (e.g., Tseng et
268 al., 1996; Smidt et al., 2005), could be observed in non-calcified *E. coli* cells heat-treated at 300°C for 20
269 h. Infrared absorption of non-calcified *E. coli* cells heated at higher temperature (600°C for 20 h) could
270 not be measured, since this sample highly reflected the IR beam (Fig. 4a). Such high reflectivity likely
271 traduced an important maturity level (e.g., Lis et al., 2005).

272 Amide (1652 cm^{-1} , 1540 cm^{-1} , 1237 cm^{-1}) and aliphatics (1455 cm^{-1} , 2958-2854 cm^{-1}) bands could
273 be observed in the FT-IR spectrum of initial calcified *E. coli* cells, although this spectrum was dominated
274 by the characteristic PO_4^{3-} absorption bands at 565, 603 and 1035 cm^{-1} (bending and stretching modes of
275 P-O groups and stretching and vibrational modes of OH^- groups) (Fig. 4b), indicative of the Ca-phosphate
276 minerals encrusting the cells (e.g., Pleshko et al., 1991; Bazin et al., 2012). Additional weak features at
277 1455 cm^{-1} and 1415 cm^{-1} were attributed to aliphatic and aromatic carbons, respectively (e.g., Trchová
278 and Stejskal, 2011). Interestingly, the FT-IR spectra of calcified *E. coli* cells did not change significantly
279 during thermal treatment at 300 or 600°C in contrast to non-calcified *E. coli* cells. The FT-IR spectrum of
280 calcified *E. coli* cells heat-treated at 600°C for 20 h appeared quite similar to the FT-IR spectrum of initial
281 calcified *E. coli* cells, despite a slight decrease of the relative intensities of amide bands and a slight
282 increase of the relative intensities of aliphatic (1455 cm^{-1}) and aromatic (1415 cm^{-1}) bands (Fig. 4b).
283 Noteworthy, the peaks corresponding to amide functional groups were still detected even after thermal
284 treatment at 600°C for 20 h and their presence interpreted as resulting from the (partial) preservation of
285 the original molecular signatures of original biomolecules.

286

287 4. Discussion

288 4.1 Impact of biomineralization on the preservation of bacteria

289 Calcified *E. coli* cells were morphologically and chemically better preserved upon heating than non-
290 calcified *E. coli* cells. This result was clearly evidenced by electron microscopy, EPR and FT-IR data.
291 Calcified cells heat-treated at 600°C for 20 h exhibited a wider EPR spectrum than non-calcified cells,
292 with ΔB_{pp} of 0.441 mT and R_{10} factor of 0.82 (Figs. 1 and 2) which is typical of low maturity organic
293 matter (Skrzypczak-Bonduelle et al., 2008). Consistently, FT-IR spectroscopy evidenced the slight
294 chemical transformations of calcified *E. coli* cells with increasing temperature compared to the strong
295 transformations undergone by non-calcified *E. coli* cells (Fig. 4).

296 The pervasive Ca-phosphate precipitation within the cell structures can explain the better
297 morphological preservation of the cells during heating as it may have provided a mechanical resistance. In
298 addition to a morphological preservation, the present study also evidenced the chemical preservation of
299 calcified *E. coli* cells upon heating. A similar chemical resistance to thermal treatments was recently
300 evidenced in experiments performed on bio-encrusted cells of iron-oxidizing bacteria, which formed
301 amorphous iron phosphate minerals within the cell walls (Li J. H. et al., 2013). Periplasmic encrustation
302 by Ca-phosphates as observed here has been suggested to be a widespread mechanism (e.g., Goulhen et
303 al., 2006; Benzerara et al., 2008; Miot et al., 2009, 2011; Cosmidis et al., 2013; Li J. H. et al., 2013) and
304 may cause sorption and entrapment of organic molecules such as peptidoglycan proteins and
305 polysaccharides on/within minerals (e.g., Miot et al., 2009, 2011). Such organic-mineral complexes may

306 facilitate the preservation of bacterial cell ultrastructural details, and potentially their chemical signatures,
307 by shielding and protecting organic molecules from reactive solutions and/or oxidizing gas phases.

308 This mechanism remains hypothetical and deserves further experimental work. However, the present
309 observations can be related to numerous previous reports that showed that even poorly resistant organic
310 molecules such as amino acids or polysaccharides can be preserved during diagenesis if encapsulated
311 within mineral biostructures such as coral skeletons and diatoms (e.g., Ingalls et al., 2003a, 2003b) or
312 microbialites (e.g., Benzerara et al., 2006; Kaur et al., 2011). A major role for minerals in organic matter
313 protection has also been recognized for soils and the occurrence of adsorptive protection of organic
314 compounds as molecular monolayers onto clay minerals has been shown to be efficient against diagenetic
315 degradation (e.g., Hedges and Keil, 1995; Ransom et al., 1998; Vandenbroucke and Largeau, 2007).

316

317 **4.2 Comparison with field sample spectroscopic signatures**

318 Extrapolating laboratory results to natural processes remains difficult, notably because geological
319 durations cannot be replicated in the laboratory. Temperatures and heating rates considerably higher than
320 those encountered in nature have traditionally been applied to laboratory samples to compensate for long
321 geological time periods (e.g., Vandenbroucke and Largeau, 2007).

322 Here, non-calcified *E. coli* cells experimentally heat-treated at 600°C for 20 h exhibited a Raman
323 spectrum which appeared markedly different from spectra of organic carbons having experienced
324 diagenetic burial in natural settings, but pretty similar to spectra from soots or charcoals, i.e. organic
325 residues having experienced only a short (on geological timescale) thermal treatment in nature.
326 Furthermore, the high reflectivity of this sample as highlighted by FT-IR spectroscopy indicated a
327 relatively high maturity (e.g., Lis et al., 2005). In addition, this sample exhibited a supra-Lorentzian EPR
328 line shape (close to 2-D dipolar) with a R_{10} factor of -1.85, similar to the EPR lineshape shown by natural
329 organic matter detected in the Apex cherts (ca. 3460 Myr) from Pilbara craton in Australia (e.g., the R_{10}
330 factor is -1.98), which is thought to have experienced metamorphic conditions in the Prehnite-Pumpellyite
331 facies to lower Greenschist facies, i.e. temperature conditions of about 200-300°C (Skrzypczak-Bonduelle
332 et al., 2008). Last, the absence in the C-XANES spectrum of *E. coli* cells heat-treated at 600°C for 20 h of
333 a sharp $1s \rightarrow \sigma^*$ exciton at 291.7 eV, related to the presence of extensive planar domains of highly
334 conjugated aromatic layers (Ahuja et al., 1996; Bernard et al., 2010), suggested that the aromatic cluster
335 size of these residues did not significantly increase even after having experienced such temperature
336 conditions. Overall, this C-XANES spectrum appeared similar to C-XANES spectra of overmature
337 kerogens (Bernard et al., 2012), i.e., kerogens having experienced a thermal history with a maximum
338 temperature of about 200-250°C.

339 Altogether, Raman, FT-IR, EPR and C-XANES data obtained on non-calcified *E. coli* cells heat-
340 treated at 600°C for 20 hours provide contrasted views when compared to natural carbons: they looked
341 like natural samples that have experienced short thermal pulse for Raman; less than 200-250°C for EPR
342 and XANES. Difficulties to relate directly the products from laboratory experiments with field samples
343 partly come from the heating rate and pressure conditions at which the present experiments were
344 conducted. Heating rate and pressure have indeed been shown to be key factors impacting the kerogen
345 decomposition rate (Beysac et al., 2003; Vandenbroucke and Largeau, 2007). In addition, organic
346 maturation processes in natural low-temperature systems may also be strongly affected by the presence of
347 water (Seewald et al., 2000; Lewan and Roy, 2011), which was rapidly lost in the present experiments.
348 Therefore, it will be important in the future to document further whether the differential evolution
349 between calcified and non-calcified *E. coli* cells detected here may also take place when these additional
350 parameters (e.g., heating rates, pressure and water) are involved.

351

352 **Concluding remarks**

353 In the present study, we investigated experimentally the impact of early encrustation by biominerals
354 on the morphological and chemical transformations of *E. coli* cells upon heating. While in the absence of
355 biominerals, *E. coli* cells were almost totally degraded, calcified *E. coli* were better preserved,
356 morphologically and chemically, during thermal treatment at 300 or 600°C, for durations as long as 100 h.
357 Such results clearly evidence the influence of bio-encrustation on bacteria preservation potential during
358 fossilization processes. The resistance of such organic-mineral complexes to diagenesis clearly illustrates
359 why self-encrusting microorganisms should be considered as pertinent targets for the search for evidence
360 of ancient life in the fossil record.

361

362 **Acknowledgements**

363 We gratefully acknowledge supports from the Simone and Cino Del Duca Foundation and the ERC
364 projects [Calcyan (Leaded by K. Benzerara) and PaleoNanoLife (Leaded by F. Robert)]. The SEM and
365 TEM experiments have been performed at the IMPMC (CNRS-UPMC, Paris). The JEOL JEM2100F at
366 the IMPMC was supported by Region Ile de France grant SESAME 2000 E 1435, INSU CNRS, INP
367 CNRS and University Pierre et Marie Curie Paris 6. The focused ion beam (FIB) and SEM facilities of
368 the IMPMC were supported by Region Ile de France grant SESAME 2006 I-07-593/R, INSU-CNRS,
369 INP-CNRS, University Pierre et Marie Curie Paris 6. STXM data were acquired at beamline 5.3.2.2 at the
370 ALS, which is supported by the Director of the Office of Science, Department of Energy, under Contract
371 No. DE-AC02-05CH11231, and at beamline 10ID-1 at the CLS, which is supported by the NSERC, the
372 CIHR, the NRC, and the University of Saskatchewan. Special thanks go to David Kilcoyne for his expert

373 support of the STXM at the ALS and to Chithra Karunakaran and Jian Wang for their expert support of
374 the STXM at the CLS.
375

- 377 Ahuja, R., Bruhwiler, P.A., Wills, J.M., Johansson, B., Martensson, N., Eriksson, O., 1996. Theoretical
378 and experimental study of the graphite 1s x-ray absorption edges. *Phys. Rev. B* 54, 14396-14404.
- 379 Bazin, D., Daudon, M., Combes, C., Rey, C., 2012. Characterization and some physicochemical aspects
380 of pathological microcalcifications. *Chem. Rev.* 112, 5092-5120.
- 381 Benning, L.G., Phoenix, V.R., Yee, N., Konhauser, K.O., 2004. The dynamics of cyanobacterial
382 silicification: An infrared micro-spectroscopic investigation. *Geochim. Cosmochim. Acta* 68,
383 743-757.
- 384 Benzerara, K., Menguy, N., Lopez-Garcia, P., Yoon, T.H., Kazmierczak, J., Tyliczszak, T., Guyot, F.,
385 Brown, G.E., 2006. Nanoscale detection of organic signatures in carbonate microbialites. *Proc.*
386 *Natl. Acad. Sci. U. S. A.* 103, 9440-9445.
- 387 Benzerara, K., Morin, G., Yoon, T.H., Miot, J., Tyliczszak, T., Casiot, C., Bruneel, O., Farges, F., Brown,
388 G.E., 2008. Nanoscale study of As biomineralization in an acid mine drainage system. *Geochim.*
389 *Cosmochim. Acta* 72, 3949-3963.
- 390 Benzerara, K., Yoon, T.H., Tyliczszak, T., Constantz, B., Spormann, A.M., Brown, G.E., 2004. Scanning
391 transmission X-ray microscopy study of microbial calcification. *Geobiology* 2, 249-259.
- 392 Bernard, S., Beyssac, O., Benzerara, K., 2008. Raman mapping using advanced line-scanning systems:
393 Geological applications. *Appl. Spectrosc.* 62, 1180-1188.
- 394 Bernard, S., Beyssac, O., Benzerara, K., Findling, N., Tzvetkov, G., Brown, G.E., Jr., 2010. XANES,
395 Raman and XRD study of anthracene-based cokes and saccharose-based chars submitted to high-
396 temperature pyrolysis. *Carbon* 48, 2506-2516.
- 397 Bernard, S., Horsfield, B., Schulz, H.M., Wirth, R., Schreiber, A., Sherwood, N., 2012. Geochemical
398 evolution of organic-rich shales with increasing maturity: A STXM and TEM study of the
399 Posidonia Shale (Lower Toarcian, northern Germany). *Mar. Pet. Geol.* 31, 70-89.
- 400 Beyssac, O., Brunet, F., Petitet, J.-P., Goffe, B., Rouzaud, J.-N., 2003. Experimental study of the
401 microtextural and structural transformations of carbonaceous materials under pressure and
402 temperature. *Eur. J. Mineral.* 15, 937-952
- 403 Beyssac, O., Lazzeri, M., 2012. Application of Raman spectroscopy to the study of graphitic carbons in
404 the Earth Sciences. In: *Applications of Raman Spectroscopy to Earth Sciences and Cultural*
405 *Heritage* (J. Dubessy, M.-C. Caumon and F. Rull, editors). *EMU Notes in Mineralogy*, 12, 415-
406 454. European Mineralogical Union and the Mineralogical Society of Great Britain & Ireland.
- 407 Bluhm, H., Andersson, K., Araki, T., Benzerara, K., Brown, G.E., Dynes, J.J., Ghosal, S., Gilles, M.K.,
408 Hansen, H.C., Hemminger, J.C., Hitchcock, A.P., Ketteler, G., Kilcoyne, A.L.D., Kneedler, E.,
409 Lawrence, J.R., Leppard, G.G., Majzlan, J., Mun, B.S., Myneni, S.C.B., Nilsson, A., Ogasawara,
410 H., Ogletree, D.F., Pecher, K., Salmeron, M., Shuh, D.K., Tonner, B., Tyliczszak, T., Warwick,
411 T., Yoon, T.H., 2006. Soft X-ray microscopy and spectroscopy at the molecular environmental
412 science beamline at the Advanced Light Source. *J. Electron. Spectrosc. Relat. Phenom.* 150, 86-
413 104.
- 414 Bourbin, M., Gourier, D., Derenne, S., Binet, L., Le Du, Y., Westall, F., Kremer, B., Gautret, P., 2013.
415 Dating carbonaceous matter in archean cherts by electron paramagnetic resonance. *Astrobiology*
416 13, 151-162.
- 417 Brasier, M.D., Green, O.R., Jephcoat, A.P., Kleppe, A.K., Van Kranendonk, M.J., Lindsay, J.F., Steele,
418 A., Grassineau, N.V., 2002. Questioning the evidence for Earth's oldest fossils. *Nature* 416, 76-81.
419
- 420 Brasier, M.D., Wacey, D., 2012. Fossils and astrobiology: New protocols for cell evolution in deep time.
421 *Int. J. Astrobiol.* 11, 217-228.
- 422 Chan, C.S., Fakra, S.C., Emerson, D., Fleming, E.J., Edwards, K.J., 2011. Lithotrophic iron-oxidizing
423 bacteria produce organic stalks to control mineral growth: implications for biosignature formation.
424 *Isme Journal* 5, 717-727.

425 Cosmidis, J., Benzerara, K., Soft X-ray scanning transmission micro-spectroscopy, in: Gower, L., DiMasi,
426 E., (Eds), Handbook of Biomineralization, Taylor and Francis, London, 2014.

427 Cosmidis, J., Benzerara, K., Gheerbrant, E., Estève, I., Bouya, B., Amaghazaz, M., 2013. Nanometer-scale
428 characterization of exceptionally preserved bacterial fossils in Paleocene phosphorites from
429 Ouled Abdoun (Morocco). *Geobiology* 11, 139-153.

430 Cuisinier, F., Bres, E.F., Hemmerle, J., Voegel, J.C., Frank, R.M., 1987. Transmission electron
431 microscopy of lattice planes in human alveolar bone apatite crystals. *Calcif. Tissue Int.* 40, 332-
432 338.

433 Filip, Z., Herman, S., Demnerova, K., 2008. FT-IR Spectroscopic characteristics of differently cultivated
434 *Escherichia coli*. *Czech J. Food Sci.* 26, 458-463.

435 Filip, Z., Herrmann, S., Kubat, J., 2004. FT-IR spectroscopic characteristics of differently cultivated
436 *Bacillus subtilis*. *Microbiol. Res.* 159, 257-262.

437 García-Ruiz, J.M., Hyde, S.T., Carnerup, A.M., Christy, A.G., Van Kranendonk, M.J., Welham, N.J.,
438 2003. Self-assembled silica-carbonate structures and detection of ancient microfossils. *Science*
439 302, 1194-1197.

440 Goulhen, F., Gloter, A., Guyot, F., Bruschi, M., 2006. Cr(VI) detoxification by *Desulfovibrio vulgaris*
441 strain Hildenborough: Microbe-metal interactions studies. *Appl. Microbiol. Biot.* 71, 892-897.

442 Gourier, D., Binet, L., Sczypczak, A., Derenne, S., Robert, F., 2004. Search for EPR markers of the
443 history and origin of the insoluble organic matter in extraterrestrial and terrestrial rocks.
444 *Spectrochim Acta A Mol. Biomol. Spectrosc.* 60, 1349-1357.

445 Gupta, N.S., Michels, R., Briggs, D.E.G., Evershed, R.P., Pancost, R.D., 2006. The organic preservation
446 of fossil arthropods: An experimental study. *Proc. R. Soc. B-Biol. Sci.* 273, 2777-2783.

447 Hedges, J.I., Keil, R.G., 1995. Sedimentary organic matter preservation: an assessment and speculative
448 synthesis. *Mar. Chem.* 49, 81-115.

449 Ingalls, A.E., Lee, C., Druffel, E.R.M., 2003a. Preservation of organic matter in mound-forming coral
450 skeletons. *Geochim. Cosmochim. Acta* 67, 2827-2841.

451 Ingalls, A.E., Lee, C., Wakeham, S.G., Hedges, J.I., 2003b. The role of biominerals in the sinking flux
452 and preservation of amino acids in the Southern Ocean along 170 degrees W. *Deep-Sea Res. Pt II*
453 50, 713-738.

454 Kaur, G., Mountain, B.W., Hopmans, E.C., Pancost, R.D., 2011. Preservation of microbial lipids in
455 geothermal sinters. *Astrobiology* 11, 259-274.

456 Kaznatcheev, K.V., Karunakaran, C., Lanke, U.D., Urquhart, S.G., Obst, M., Hitchcock, A.P., 2007. Soft
457 X-ray spectromicroscopy beamline at the CLS: Commissioning results. *Nucl. Instrum. Meth. A*
458 582, 96-99.

459 Kilcoyne, A.L.D., Tyliczszak, T., Steele, W.F., Fakra, S., Hitchcock, P., Franck, K., Anderson, E.,
460 Harteneck, B., Rightor, E.G., Mitchell, G.E., Hitchcock, A.P., Yang, L., Warwick, T., Ade, H.,
461 2003. Interferometer-controlled scanning transmission X-ray microscopes at the Advanced Light
462 Source. *J. Synchrotron Radiat.* 10, 125-136.

463 Konhauser, K., Riding, R., Bacterial Biomineralization, in: Knoll, H., Canfield, D.E., Konhauser, K.O.,
464 (Eds), Fundamentals of Geobiology, John Wiley & Sons, Ltd, 2012, pp. 105-130, doi:
465 110.1002/9781118280874.ch9781118280878.

466 Lahfid, A., Beyssac, O., Deville, E., Negro, F., Chopin, C., Goffé, B., 2010. Evolution of the Raman
467 spectrum of carbonaceous material in low-grade metasediments of the Glarus Alps (Switzerland).
468 *Terra Nova* 22, 354-360.

469 Lalonde, S.V., Konhauser, K.O., Reysenbach, A.L., Ferris, F.G., 2005. The experimental silicification of
470 Aquificales and their role in hot spring sinter formation. *Geobiology* 3, 41-52.

471 Lewan, M.D., Roy, S., 2011. Role of water in hydrocarbon generation from Type-I kerogen in Mahogany
472 oil shale of the Green River Formation. *Org. Geochem.* 42, 31-41.

473 Li, J.H., Benzerara, K., Bernard, S., Beyssac, O., 2013a. The link between biomineralization and
474 fossilization of bacteria: Insights from field and experimental studies. *Chem. Geol.* 359, 49-69.

475 Li, J.H., Pan, Y.X., Liu, Q.S., Yu-Zhang, K., Menguy, N., Che, R.C., Qin, H.F., Lin, W., Wu, W.F.,
 476 Petersen, N., Yang, X.A., 2010. Biomineralization, crystallography and magnetic properties of
 477 bullet-shaped magnetite magnetosomes in giant rod magnetotactic bacteria. *Earth Planet. Sci. Lett.*
 478 293, 368-376.

479 Li, Y.L., Konhauser, K.O., Kappler, A., Hao, X.L., 2013b. Experimental low-grade alteration of biogenic
 480 magnetite indicates microbial involvement in generation of banded iron formations. *Earth Planet*
 481 *Sc. Lett.* 361, 229-237.

482 Lis, G.P., Mastalerz, M., Schimmelmann, A., Lewan, M.D., Stankiewicz, B.A., 2005. FTIR absorption
 483 indices for thermal maturity in comparison with vitrinite reflectance R₀ in type-II kerogens from
 484 Devonian black shales. *Org. Geochem.* 36, 1533-1552.

485 Lowenstam, H.A., 1981. Minerals formed by organisms. *Science* 211, 1126-1131.

486 Miot, J., Benzerara, K., Kappler, A., 2014. Investigating microbe–mineral interactions: Recent advances
 487 in X-ray and electron microscopy and redox-sensitive methods. *Annu. Rev. Earth Pl. Sc.* 42, In
 488 press.

489 Miot, J., Benzerara, K., Morin, G., Kappler, A., Bernard, S., Obst, M., Ferard, C., Skouri-Panet, F.,
 490 Guigner, J.M., Posth, N., Galvez, M., Brown, G.E., Guyot, F., 2009. Iron biomineralization by
 491 anaerobic neutrophilic iron-oxidizing bacteria. *Geochim. Cosmochim. Acta* 73, 696-711.

492 Miot, J., Maclellan, K., Benzerara, K., Boisset, N., 2011. Preservation of protein globules and
 493 peptidoglycan in the mineralized cell wall of nitrate-reducing, iron(II)-oxidizing bacteria: a cryo-
 494 electron microscopy study. *Geobiology* 9, 459-470.

495 Mrozowski, S., 1988. ESR Studies of carbonization and coalification processes Part II. Biological
 496 materials. *Carbon* 26, 531-541.

497 Oehler, J.H., Schopf, J.W., 1971. Artificial microfossils: Experimental studies of permineralization of
 498 blue-green algae in silica. *Science* 174, 1229-1231.

499 Orange, F., Westall, F., Disnar, J.R., Prieur, D., Bienvenu, N., Leromancer, M., Defarge, C., 2009.
 500 Experimental silicification of the extremophilic Archaea *Pyrococcus abyssi* and
 501 *Methanocaldococcus jannaschii*: Applications in the search for evidence of life in early Earth and
 502 extraterrestrial rocks. *Geobiology* 7, 403-418.

503 Paris, C., Lecomte, S., Coupry, C., 2005. ATR-FTIR spectroscopy as a way to identify natural protein-
 504 based materials, tortoiseshell and horn, from their protein-based imitation, galalith. *Spectrochim.*
 505 *Acta A: Mol. Biomol. Spectrosc.* 62, 532-538.

506 Papineau, D., De Gregorio, B.T., Stroud, R.M., Steele, A., Pecoits, E., Konhauser, K., Wang, J.H., Fogel,
 507 M.L., 2010. Ancient graphite in the Eoarchean quartz-pyroxene rocks from Akilia in southern
 508 West Greenland II: Isotopic and chemical compositions and comparison with Paleoproterozoic
 509 banded iron formations. *Geochim. Cosmochim. Acta* 74, 5884-5905.

510 Pleshko, N., Boskey, A., Mendelsohn, R., 1991. Novel infrared spectroscopic method for the
 511 determination of crystallinity of hydroxyapatite minerals. *Biophys. J.* 60, 786-793.

512 Ransom, B., Kim, D., Kastner, M., Wainwright, S., 1998. Organic matter preservation on continental
 513 slopes: Importance of mineralogy and surface area. *Geochim. Cosmochim. Acta* 62, 1329-1345.

514 Ravel, B., Newville, M., 2005. ATHENA, ARTEMIS, HEPHAESTUS: data analysis for X-ray
 515 absorption spectroscopy using IFEFFIT. *J. Synchrotron Radiat.* 12, 537-541.

516 Sadezky, A., Muckenhuber, H., Grothe, H., Niessner, R., Pöschl, U., 2005. Raman microspectroscopy of
 517 soot and related carbonaceous materials: Spectral analysis and structural information. *Carbon* 43,
 518 1731-1742.

519 Seewald, J.S., 2001. Aqueous geochemistry of low molecular weight hydrocarbons at elevated
 520 temperatures and pressures: Constraints from mineral buffered laboratory experiments. *Geochim.*
 521 *Cosmochim. Acta* 65, 1641-1664.

522 Skrzypczak-Bonduelle, A., Binet, L., Delpoux, O., Vezin, H., Derenne, S., Robert, F., Gourier, D., 2008.
 523 EPR of radicals in primitive organic matter: A tool for the search of biosignatures of the most
 524 ancient traces of life. *Appl. magn. Reson.* 33, 371-397.

525 Solomon, D., Lehmann, J., Kinyangi, J., Liang, B.Q., Heymann, K., Dathe, L., Hanley, K., Wirick, S.,
526 Jacobsen, C., 2009. Carbon (1s) NEXAFS spectroscopy of biogeochemically relevant reference
527 organic compounds. *Soil Sci. Soc. Am. J.* 73, 1817-1830.

528 Stankiewicz, B.A., Briggs, D.E.G., Michels, R., Collinson, M.E., Flannery, M.B., Evershed, R.P., 2000.
529 Alternative origin of aliphatic polymer in kerogen. *Geology* 28, 559-562.

530 Studier, F.W., Moffatt, B.A., 1986. Use of bacteriophage T7 RNA polymerase to direct selective high-
531 level expression of cloned genes. *J. Mol. Biol.* 189, 113-130.

532 Toporski, J.K.W., Steele, A., Westall, F., Thomas-Keprta, K.L., McKay, D.S., 2002. The simulated
533 silicification of bacteria: New clues to the modes and timing of bacterial preservation and
534 implications for the search for extraterrestrial microfossils. *Astrobiology* 2, 1-26.

535 Trchová, M., Stejskal, J., 2011. Polyaniline: The infrared spectroscopy of conducting polymer nanotubes
536 (IUPAC Technical Report). *Pure Appl. Chem.* 83, 1803-1817.

537 Van Zuilen, M.A., Chaussidon, M., Rollion-Bard, C., Marty, B., 2007. Carbonaceous cherts of the
538 Barberton Greenstone Belt, South Africa: Isotopic, chemical and structural characteristics of
539 individual microstructures. *Geochim. Cosmochim. Acta* 71, 655-669.

540 Vandenbroucke, M., Largeau, C., 2007. Kerogen origin, evolution and structure. *Org. Geochem.* 38, 719-
541 833.

542 Watson, J.S., Fraser, W.T., Sephton, M.A., 2012. Formation of a polyalkyl macromolecule from the
543 hydrolysable component within sporopollenin during heating/pyrolysis experiments with
544 Lycopodium spores. *J. Anal. Appl. Pyrolysis* 95, 138-144.

545 Weiner, S., Dove, P.M., 2003. An overview of biomineralization processes and the problem of the vital
546 effect. *Biomineralization* 54, 1-29.

547 Westall, F., Boni, L., Guerzoni, E., 1995. The experimental silicification of microorganisms.
548 *Palaeontology* 38, 495-528.

549 Yule, B.L., Roberts, S., Marshall, J.E.A., 2000. The thermal evolution of sporopollenin. *Org. Geochem.*
550 31, 859-870.

551

552 **Figure captions**

553

554 Figure 1. Morphological alteration of non-calcified *E. coli* cells (a and b) and calcified *E. coli* cells (c and
555 d) after heating treatments. (a) TEM image of *E. coli* cells dehydrated at room-temperature for two weeks.
556 (b) TEM image of *E. coli* cells heated at 300°C for 2 h. The morphological structure of *E. coli* cells was
557 completely lost after heating at 300 or 600°C, even in the 2-h long experiments. (c) SEM and TEM (inset)
558 image of calcified *E. coli* cells dehydrated at room-temperature. (d) SEM and TEM (inset) image of
559 calcified *E. coli* heated at 600°C for 20 h. SEM and TEM analyses show that the *E. coli* cells were heavily
560 aggregated and encrusted by whisker-shaped minerals, and that the morphological structures including
561 encrusted cells (indicated by single-ended arrow with a solid line) and cell aggregates were well
562 preserved after all heating experiments.

563

564 Figure 2. (a) Raman spectrum of non-calcified *E. coli* cells heat at 600°C for 20 h. The spectrum was
565 deconvoluted with a four-band fitting (*G*, *D1*, *D2* and *D3*) using a Voigt profile, as described in Beysnac
566 et al. (2002). (b) EPR spectra of non-calcified and calcified *E. coli* cells heat-treated at 600°C for 20 h. (c)
567 Description of the EPR line shape of the two samples. ΔB_{pp} and A_{pp} indicate the peak-to-peak line width
568 and amplitude, respectively, ΔB is the magnetic field offset from the line center, and A is EPR amplitude
569 values at each point of the EPR line. The line shape parameter R_{10} , which was calculated following
570 Skrzypczak-Bonduelle et al. (2008), is used to quantify the deviations of the experimental points from the
571 Lorentzian shape in this plot.

572

573 Figure 3. C K-edge XANES spectra of heat-treated *E. coli* cells. The peaks at 285.2 eV, 287.3 eV, 287.8
574 eV, 288.2 eV, 288.5 eV, and 289.4 eV correspond to electronic transitions in aromatic (C=C), alcohol (C-
575 O), aliphatics (C-C), amide (O=C-NH_x), carboxyl (O=C-O), and alcohol (C-O) functional groups,
576 respectively. The peaks at 297.3 eV and 300 eV correspond to the potassium *L*_{2,3}-edges indicating the
577 presence of K most likely precipitated from the culture medium.

578

579 Figure 4. Infrared spectra of non-heated and thermally treated samples of non-calcified (a) and calcified
580 (b) *E. coli* cells. The bands at 2958-2854 cm⁻¹ correspond to C-H stretching in aliphatics. The peak 1702
581 cm⁻¹ corresponds to C-O stretch of CO₂H, 1655/1652 cm⁻¹ to amide I, 1628 cm⁻¹ to aromatic band C=C,
582 1540 cm⁻¹ to amide II, 1455 cm⁻¹ to C-H deformations of CH₂ or CH₃ groups in aliphatics, 1393 cm⁻¹ to
583 C-H bending, 1265 cm⁻¹ to C=O stretch of -COOH, 1237 cm⁻¹ to amide III, 1082 cm⁻¹ to C=O stretching.
584 The peaks at 565 cm⁻¹ and 603 cm⁻¹ correspond to P-O-P bending, and 1035 cm⁻¹ to P-O stretching of PO₄

585 groups, or to the vibrational modes of OH⁻ groups. The small peaks at 1093 cm⁻¹ and 962 cm⁻¹ correspond
586 to P-O-P bending.
587

588 **Supplementary Figure Captions**

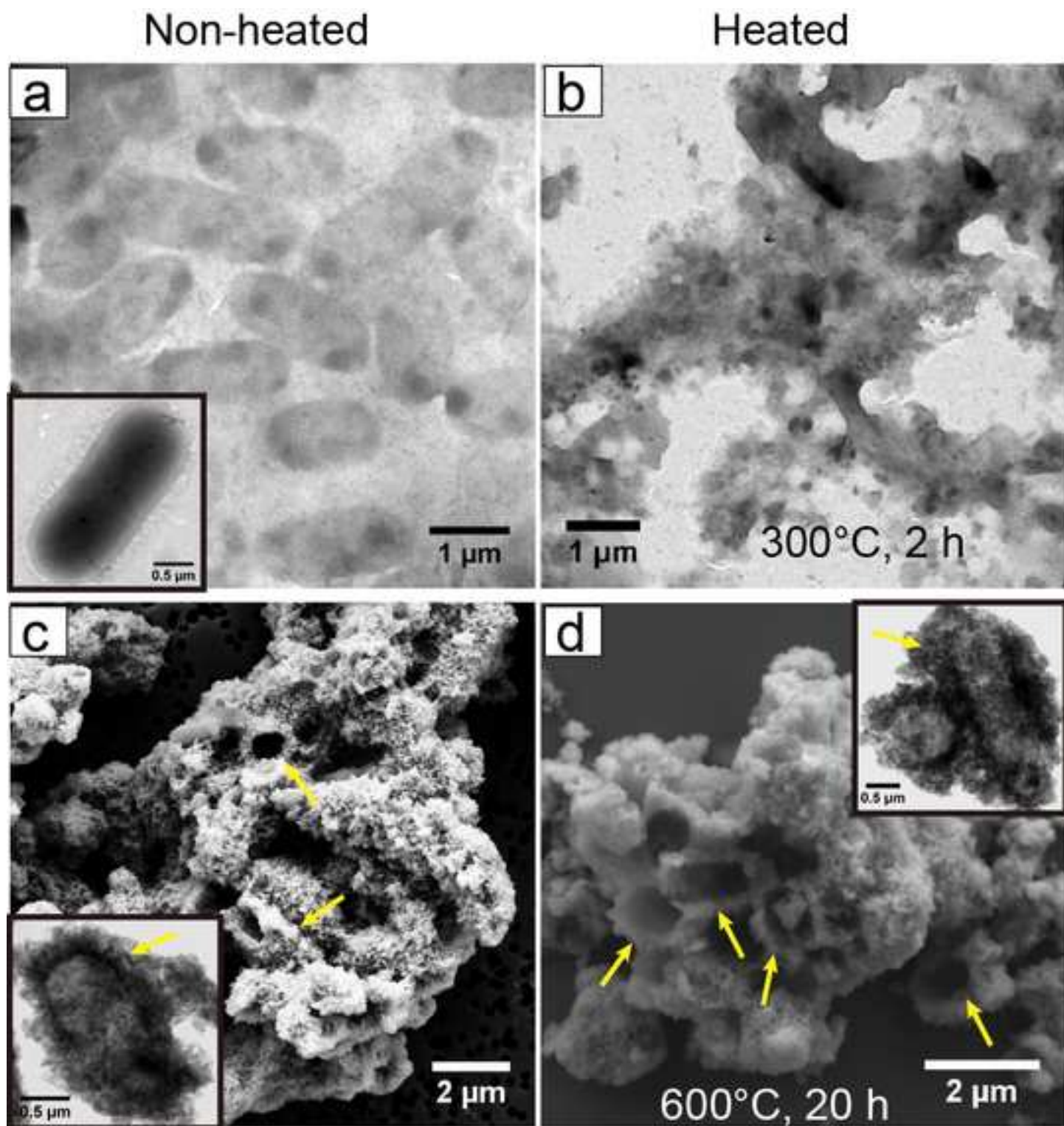
589

590 Figure S1. Morphological and chemical characterization of non-heated calcified *E. coli* cells. (a) SEM
591 image of heavily encrusted and aggregated calcified *E. coli* cells. (b) STEM image showing minerals
592 located within the cells, within the cell walls and at the cell surfaces. (c) TEM image showing the high
593 amount of minerals at the cell surface. (d)-(i) STEM-XEDS maps showing the spatial distribution of C, O,
594 P and Ca. (j) SAED pattern of the Ca-phosphate minerals. The d-spacing values calculated from two
595 major electron diffraction rings are 3.44 and 2.75 Å, which can be indexed as the (002) and (121) lattice
596 planes of hydroxyapatite, respectively. (k) HRTEM image of hydroxyapatite crystals.

597

598 Figure S2 Morphological and chemical characterization of calcified *E. coli* cells after heated at 600°C for
599 20 h. (a) SEM image. (b) STEM image. (c) TEM image. (d)-(i) STEM-XEDS maps of C, O, P and Ca. (i)
600 SAED pattern showing the Ca-phosphate minerals are still hydroxyapatite. (k) HRTEM image of the
601 hydroxyapatite minerals. SEM and TEM analyses altogether reveal a good morphological preservation of
602 calcified *E. coli* cells after heating treatments. SAED and HRTEM lattice imaging also show an increase
603 of crystallinity of hydroxyapatite crystals after heating treatments, e.g., sharper and narrower electron
604 diffraction rings recorded from the 600°C-20h-heated sample compared to the unheated one.

- (1) The biogenicity of microfossils is often debated because of morphological and chemical alteration during geological history.
- (2) We experimentally studied the effect of bacterial biomineralization on fossilization during thermal treatments.
- (3) Calcified *E. coli* were better preserved morphologically and chemically during heating up to 600°C and 100 h.
- (4) These evidence the influence of bio-encrustation on bacteria preservation potential during fossilization processes.
- (5) Self-encrusting microorganisms should be considered as pertinent targets for the search for ancient life in fossil record.



Figure

[Click here to download high resolution image](#)

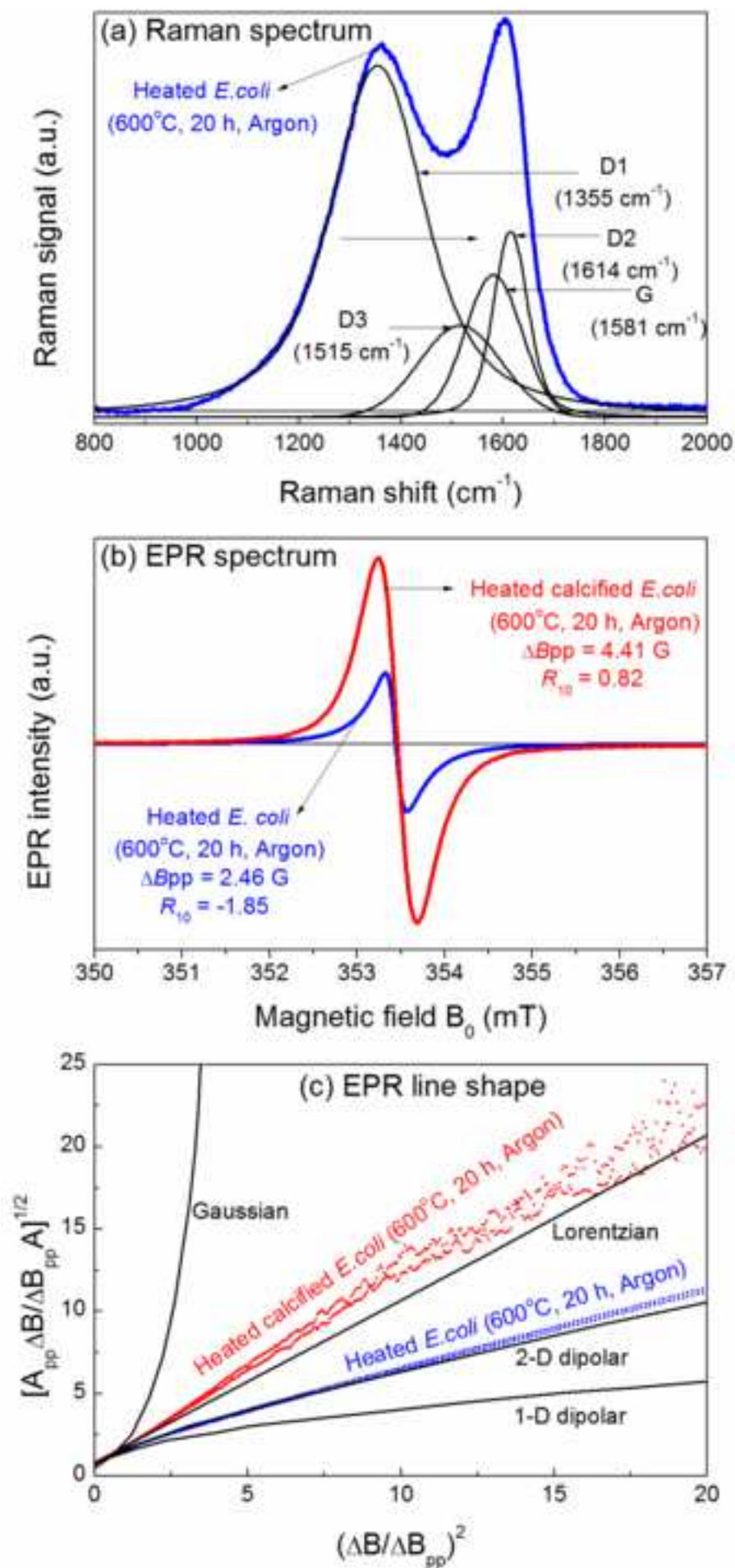
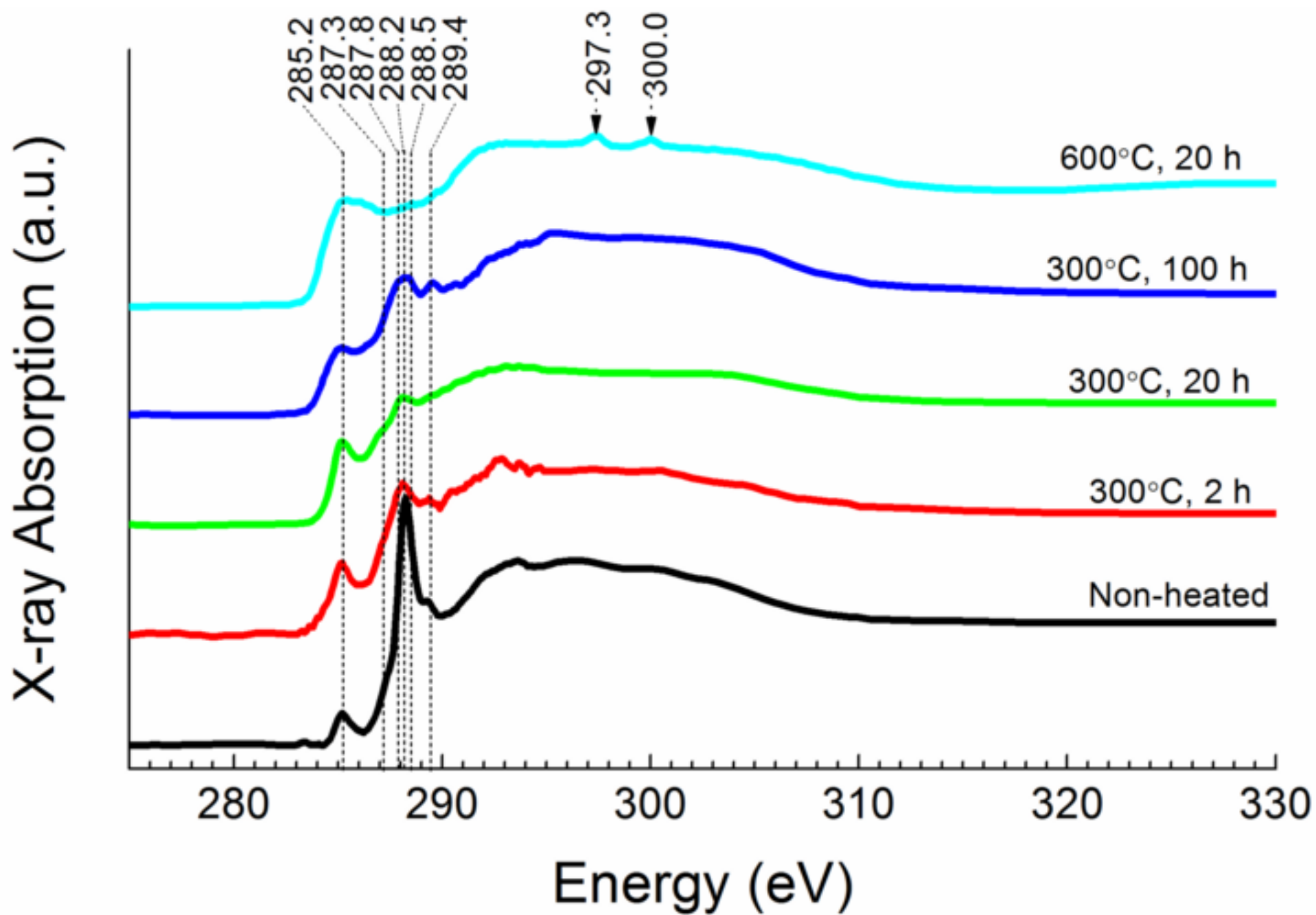


Figure
[Click here to download high resolution image](#)



Figure

[Click here to download high resolution image](#)